

## Integrated Spatial Multi-Omics Study of Postmortem Brains of Alzheimer's Disease

Yumiko Toyama<sup>1</sup>, Takashi Nirasawa<sup>2</sup>, Maho Morishima<sup>3</sup>, Yuko Saito<sup>3</sup>, Kazuhiro Irie<sup>1,4</sup>, Shigeo Murayama<sup>3</sup> and Masaya Ikegawa<sup>1</sup>

<sup>1</sup>Department of Life and Medical Systems, Doshisha University, Kyotanabe, Japan, <sup>2</sup>Bruker Japan K. K., Yokohama, Japan,

<sup>3</sup>The Brain Bank for Aging Research, Tokyo Metropolitan Geriatric Hospital and Institute of Gerontology, Tokyo, Japan and

<sup>4</sup>Division of Food Science and Biotechnology, Graduate School of Agriculture, Kyoto University, Kyoto, Japan

Received April 27, 2024; accepted May 12, 2024; published online June 28, 2024

Pathological hallmark of Alzheimer's disease (AD) is characterized by the accumulation and aggregation of amyloid  $\beta$  (A $\beta$ ) peptides into extracellular plaques of the brain. Clarification of the process of how soluble A $\beta$  starts to assemble into amyloid fibrils is an essential step in elucidating the pathogenesis of AD. In our previous study, A $\beta$  proteoforms including full-length A $\beta$ 40 and A $\beta$ 42/43 with N- and C-terminal truncated forms were visualized in post-mortem brains from AD patients with matrix-assisted laser desorption/ionization-based mass spectrometry imaging (MALDI-MSI). In this study, A $\beta$  proteoforms were consistently visualized by an updated protocol, and uncharacterized peptides such as A $\beta$ 1-29 and A $\beta$ 10-40 in AD brains were also visualized. To decipher neurotoxic effects of A $\beta$  in patients' brains, here we integrate liquid chromatography tandem mass spectrometry (LC-MS/MS) based shotgun proteomics with laser microdissection (LMD) excised tissue samples as well as direct tissue imaging with MALDI-MSI. With this approach, we have highlighted dynamic alterations of microtubule associating proteins (MAPs) including MAP1A, MAP1B and MAP2 as well as AD dominant proteins including APP, UCHL1, SNCA, and APOE. Of note, as lipid dysregulation has been implicated with AD pathology, we have challenged to integrate proteomics and lipid imaging for AD and control brain tissue. Spatial multi-omics is also valid to uncover molecular pathology of white matter as well as grey matter and leptomeningeal area, for example, by visualizing heme in patients' postmortem brains.

**Key words:** mass spectrometry imaging, Alzheimer's Disease, amyloid beta, proteomics, lipid imaging

### I. Introduction

Alzheimer's disease (AD) is the most common devastating neurodegenerative disorder characterized by the irreversible loss of memory and cognitive functions. The major pathological hallmark of AD is the accumulation and deposition of amyloid  $\beta$  (A $\beta$ ) peptides outside neurons, which was followed by the formation of intra-neuronal tangles of the protein tau. Several lines of evidence suggests that these neuropathological alterations of AD probably begin much

earlier than the appearance of clinical symptoms and production and elimination imbalance of A $\beta$  peptides will initiate the neuropathology. Thus, "amyloid cascade hypothesis" has become the major AD pathogenesis and is guiding a potential treatment [14, 37]. Although some recent success of anti-amyloid immunotherapies for AD in early clinical trials were reported, the pathogenesis of AD seems much more complex and still is not entirely understood.

Amyloid plaques were found to primarily consist of A $\beta$  peptides that are produced upon sequential, proteolytic processing of amyloid precursor protein (APP), which is an integral membrane protein [26]. Amyloid plaques are found

Correspondence to: Masaya Ikegawa, Department of Life and Medical Systems, Doshisha University, Tataramiyakodani 1-3, Kyotanabe 610-0394, Japan. E-mail: mikegawa@mail.doshisha.ac.jp

in cerebral parenchyma and deposited in vessels of AD brains long before disease onset. Over the past 40 years since their discovery [26], a high degree of A $\beta$  heterogeneity besides full-length peptides have been clarified in both brains of patients with sporadic or familial forms of AD, that are commonly delineated using immunohistochemistry that have distinct limitations with respect to specificity and sensitivity of the antibodies. Recently, matrix assisted laser desorption ionization mass spectrometry-based chemical imaging (MALDI-MSI) has been successfully introduced to comprehensively delineate spatial A $\beta$  peptide- and neuronal lipid-patterns associated with plaque pathology in brain tissue in both AD mouse models [21, 22, 39, 40] and human samples [17, 20]. This mass spectrometry-based imaging approach enabled us to overcome major limitations of commonly used biochemical methods and opens for both static and dynamic biochemical process of amyloid aggregation *in situ* [19].

A $\beta$  plaques were composed with highly ordered fibrillar aggregates of A $\beta$ s and A $\beta$  oligomers. The formation of A $\beta$  fibrils take several steps as follows: 1) oligomerization of monomeric A $\beta$ , 2) formation of protofibrils from A $\beta$  oligomers and 3) aggregation into A $\beta$  fibrils. Although A $\beta$ 42 is more neurotoxic than A $\beta$ 40, the production rate and an interplay between these A $\beta$  species might also be important in AD pathology [18, 27, 43]. Recently, an intermediate transition form of A $\beta$  has been paid much attention because of its more neurotoxic effects compared with A $\beta$  fibrils [12, 45]. Of note, due to emerging technology of cryo-electron microscopy (cryo-EM), brain-derived A $\beta$  fibrils are much more polymorphic, and the property of these A $\beta$  fibrils differ sharply than expected from *in vitro* experiments. The composition of these plaques revealed a high amount of A $\beta$  fibrils as well as a high concentration of lipids [8, 9, 10, 11, 24, 42, 46].

Considering that A $\beta$  fibrillization is modulated by multiple factors including peptide mutations, metals, and lipids in the pathogenesis of AD, spatial multi-omics study for AD is a promising approach. In this study, MALDI-MSI analysis of three AD brains and three control brains were performed for 1) intact MSI for mapping A $\beta$  proteoforms, 2) in-depth proteomics from laser micro-dissected tissue samples, 3) direct protein imaging from on tissue digested brain tissues and 4) lipid imaging to gain insights into A $\beta$ -mediated lipidomic pathogenesis. Again, as lipid membranes will promote A $\beta$  fibrillization and aggregation on its surface, and then followed by altered membrane integrity and permeability as the consequences of A $\beta$ -mediated neurotoxicity, here we dissect a variety of A $\beta$  proteoforms and its related proteins and lipids *in situ* to shed new lights for neuropathology of AD.

## II. Materials and Methods

### Ethics statement

The brain autopsy specimens were provided by the

**Table 1.** Clinical and pathological data of AD with CAA cases and controls

Patient	Gender	Age at death	Braak Stage	CAA
1	M	84	V	3
2	M	88	V	1
3	F	87	VI	3
1	M	84	I	0
2	M	78	I	0
3	M	70	I	1

Braak stages I–II indicate early stages where neurofibrillary changes appear in the entorhinal cortex or olfactory areas of the medial temporal lobe. Subsequently, neurofibrillary changes progress to the hippocampal region, classified as Braak Stages III–IV. Braak Stages V–VI are considered final stages where neurofibrillary changes extend to associate cortices or primary cortices of the neocortex. While cognitive impairment is nearly absent in Braak Stages I–II, cases with mild cognitive impairment increase in Stages III–IV, and cognitive impairment is evident in Braak Stages V–VI.

Tokyo Metropolitan Geriatric Hospital. These tissue samples have been registered with the Brain Bank for Aging Research (BBAR). The autopsies were conducted with informed consent obtained from the deceased’s relatives. The operation of BBAR has received approval from the ethics committee at the Tokyo Metropolitan Geriatric Hospital and Institute of Gerontology. The bodies of the patients were promptly transferred to a cold environment (4°C) within two hr following their demise, aiming to minimize postmortem tissue alterations. Brain tissue samples were obtained from specimens that were removed and stored at –80°C within 8 hr postmortem. All methods described in this study have been approved by Doshisha University and BBAR at the Tokyo Metropolitan Geriatric Hospital and Institute of Gerontology. Clinical and pathological data of human brains Brain samples were collected from the occipital cortex of both sporadic AD patients (n = 3) and non-pathological controls (n = 3) of the same age group. In AD brains, the occurrence and quantity of neurofibrillary changes correlate with clinical symptoms, and Braak staging is utilized as a classification system for AD stages (Table 1). Braak staging was conducted through pathological and histological examination performed during autopsy. For the human brains obtained, the degree of A $\beta$  deposition was assessed based on the CAA score (score: 0–3) in Table 1, and the severity of AD was determined based on Braak Stage (score: I–VI).

### Sample preparation for MALDI-MSI

#### 1) Preparation of frozen tissues for non-digested imaging

In a cryostat (CM1950, Leica Microsystems, Wetzlar, Germany), the frozen tissue sections were cut at 10–20  $\mu$ m thickness and mounted onto indium tin oxide (ITO)-coated glass slides (Bruker Daltonics, Bremen, Germany) for MALDI-MSI. The tissue slice was thawed by placing a finger on the non-ITO-coated side of the slide at room temperature and vacuum drying was performed for 20 min. The samples were then sequentially immersed in 70% ethanol

for 30 sec, 100% ethanol for 30 sec, and Carnoy's solution (six parts of 100% ethanol, three parts acetic acid and one part chloroform) for 2 min to remove endogenous lipids and inorganic salts. Then followed by 30 sec in 100% ethanol, 1 min in 0.1% trifluoroacetic acid solution (TFA, FUJIFILM Wako) and 30 sec in 100% ethanol. After the washing process, the samples were vacuum dried for 30 min. Prior to matrix coating, the samples were treated with 100% formic acid vapor at 60°C for 6 min. This step is applicable only for the detection of intact A $\beta$ . The matrix coating on the slides was performed using the TM-Sprayer (HTX Technologies). For non-digested tissues, 15 mg/ml of 2,5-dihydroxybenzoic acid (DHB, Bruker Daltonics) in 90% acetonitrile with 0.1% TFA was used as matrix and the spray temperature was set to 60°C.

### *2) Preparation of frozen tissues for protein imaging with trypsin digestion*

A set of two serial tissue sections were prepared for each analysis, and one section from each set underwent MALDI-MSI analysis and from the other section, proteins and peptides were extracted for shotgun proteomics. After vacuum drying, the samples were washed in 70% ethanol for 30 sec, 100% ethanol for 30 sec, Carnoy's solution for 2 min, 100% ethanol for 30 sec, and 0.1% TFA for 1 min. After the washing process, the tissue sections were immersed in a 20 mM ammonium bicarbonate solution (FUJIFILM Wako) for 1 min. The samples were then sprayed with trypsin (Promega) solution (25 mg/ml in 20 mM ammonium bicarbonate, pH 7.5–8.5). This step must be done uniformly onto the tissue sections using the TM-Sprayer. Then, the tissue sections were incubated at 50°C in a 20 mM ammonium bicarbonate vapor for 120 min. After incubation, 0.1% TFA was added to cover the entire tissue. The section was incubated at room temperature for 15 min. Only the extraction solution was collected. Matrix coating was then performed using the TM-Sprayer. For trypsin-digested tissues, 10 mg/ml of  $\alpha$ -cyano-4-hydroxycinnamic acid (CHCA, Nacalai tesque, Specially Prepared Regent) in 70% acetonitrile with 1% TFA was used as matrix and the spray temperature was set to 75°C. After matrix coating, the samples were treated with 10 mM acetic acid vapor at 37°C for 5 min.

### *3) Preparation of frozen tissues for lipids imaging*

In a cryostat, the frozen tissue sections were cut at 10  $\mu$ m thickness and mounted onto ITO-coated glass slides for MALDI-MSI. The tissue slice was thawed at room temperature and underwent vacuum drying for 20 min. The matrix coating on the slides was performed using the TM-Sprayer. For lipids imaging, 15 mg/ml DHB in 90% acetonitrile with 0.1% TFA was used as matrix and the spray temperature was set to 60°C.

### **Measurement and data analysis for MALDI-MSI**

For intact protein imaging and lipids imaging, the

instrument was mass calibrated with red phosphorus. Also, for digested MALDI-MSI, Peptide Calibration Standard I (Bruker Daltonics), TA30 (3 parts of 100% acetonitrile and 7 parts of 0.1% TFA), and CHCA were mixed to prepare the calibration solution. Several 1  $\mu$ l droplets of the solution were dispensed onto the slide. Imaging analysis was performed using the rapifleX and timsTOF fleX (both Bruker Daltonics). For digested MSI, measurements were conducted in positive reflector mode with a spatial resolution of 50  $\mu$ m, covering the m/z range of 200–4,000 or 600–4,000. Conversely, for undigested MSI, measurements were conducted in positive linear mode with a spatial resolution of 50–70  $\mu$ m, covering the m/z range of 200–5,000 or 600–15,000. For lipid imaging, measurements were conducted in positive mode with a spatial resolution of 70  $\mu$ m, covering the m/z range of 100–1,400. The obtained mass spectra imaging data were visualized and analyzed using fleximaging 5.0 and SCiLS Lab 2023b software (both Bruker Daltonics).

### **Preparation of frozen samples for shotgun proteomics**

Serial tissue sections were prepared, and one of the sections was used for MALDI-MSI measurement. The other tissue section was used for shotgun proteomics as above-mentioned. The TM-Sprayer and trypsin digestion treatment by incubation were conducted for both slides. After incubation, 0.1% TFA was added to cover the entire tissue on the tissue section. The section was incubated at room temperature for 15 min. Extraction solution was collected in a tube.

### **Measurement and data analysis for shotgun proteomics**

The collected peptide extraction solution was analyzed for peptide fragments using Nano Elute and timsTOF Pro2 instruments (both from Bruker Daltonics). After centrifugation, the supernatant was diluted two-fold with a 2% acetonitrile solution containing formic acid. One microliter of the diluted solution was used for measurement. The measurements were conducted using a 25 cm  $\times$  75  $\mu$ m  $\times$  1.6  $\mu$ m C18 column (IonOptiks) at a flow rate of 400 nL/min for 120 min. Additionally, the sample solution obtained through laser microdissection, as described later, was centrifuged, and the supernatant was collected. Two microliters (2  $\mu$ l) of this sample were used for measurement, employing the same column, flow rate, and duration as previously mentioned. For protein analysis, PEAKS Studio 8.5 (Bioinformatics Solutions Inc., Ontario, Canada), ProteinScape4 (Bruker Daltonics), and MASCOT software (Matrix Science, London, UK) were utilized.

### **Preparation of tissue samples with laser microdissection (LMD)**

In a cryostat, the frozen tissue sections were cut at 10  $\mu$ m thickness and mounted onto Membrane Slides (Carl Zeiss Microscopy GmbH, Germany) for LMD. Consecutive sections from samples subjected to intact imaging were

employed. To distinguish between grey and white matter, quick-toluidine blue staining was performed using the following procedure. The sections were immersed in 5% acetic acid-containing ethanol for 3 min, followed by a 1-min immersion in MilliQ water. Subsequently, they were immersed in a 0.05% toluidine blue solution (206-14555, Wako) for 45 sec, and then immersed twice for 1 min each in MilliQ water.

#### **Liquid Chromatography Tandem Mass Spectrometry (LC-MS/MS)**

Excision from human brain tissue was performed using the PALM MicroBeam (Carl Zeiss Microscopy GmbH, Germany). The matrix-coated slides used for intact imaging were subjected to H&E staining. H&E staining enables the visualization of amyloid plaques. The H&E-stained slides were positioned beneath the membrane slides used for LMD. This alignment enabled matching amyloid-deposit locations with the microscopically recognized amyloid deposition on the LMD slides. The LMD area for protein analysis within each tube was standardized to 50  $\mu\text{m} \times 50 \mu\text{m}$ . Sections were collected onto the caps of Eppendorf tubes filled with 20 mM ammonium bicarbonate. After centrifugation, the sections were deposited at the bottom of the Eppendorf tubes. A trypsin solution dissolved in 20 mM ammonium bicarbonate was added and incubated at 37°C for 8 hr.

#### **Measurement and data analysis for shotgun proteomics**

After digestion with trypsin, the peptide extraction solution was subjected to peptide fragment measurement using Nano Elute and timsTOF Pro2. The recovered solution was centrifuged, and the supernatant was collected. The supernatant was then diluted twofold with a solution containing 2% acetonitrile and formic acid (FujiFilm Wako Pure Chemical Corporation). A 1  $\mu\text{l}$  aliquot of this diluted solution was used as the measurement sample.

Measurements were conducted using a 25 cm  $\times$  75  $\mu\text{m} \times$  1.6  $\mu\text{m}$  C18 column (IonOptiks) with a flow rate of 400 nl/min over a 120-min period. Samples recovered by LMD were centrifuged, and the supernatant was collected. Without dilution, a 2  $\mu\text{l}$  aliquot was used as the measurement sample. For data analysis, PEAKS Studio 8.5 (Bioinformatics Solutions Inc., Ontario, Canada), ProteinScape4 (Bruker Daltonics), and MASCOT software (Matrix Science, London, UK) were utilized.

**Immunohistochemistry and histology** Fresh frozen sections of human brains were fixed with 4% paraformaldehyde in phosphate buffered saline (PBS) for 30 min. The brain tissue slides were washed with PBS, 100% ethanol for 5 min each. After washing, the tissues were dipped in 98% formic acid for 5 min to enhance the detection of A $\beta$ . These tissues were blocked with 10% normal goat serum in PBS and incubated with 1  $\mu\text{g}/\text{ml}$  primary antibodies against N-terminal of A $\beta$ , 82E1 (IBL, Gunma, Japan). These sections were incubated in a humidified chamber at 4°C for 8

hr. After washing with 3 times PBS, the tissues were incubated with a secondary antibody solution (anti rabbit IgG antibody) for 2 hr in humidified chamber. After subsequent washes with PBS, an Avidin—biotin complex solution (prepared according to the kit manual from VECTOR Laboratories) was added by dropping onto the tissue sections, and the reaction was allowed to proceed for 30 min at room temperature. Following washing step with PBS-Tween20 and PBS, the sections were treated with 3,3'-diaminobenzidine (DAB) solutions. Imaging was conducted using an Olympus BX51 optical microscope.

#### **Hematoxylin and eosin staining**

The fresh frozen sections were immersed in a solution of 4% paraformaldehyde in PBS for 30 min to fix the tissues. After conducting MSI, the tissue sections were washed twice for 3 min each with 100% ethanol to remove the matrix on the tissue before tissue fixation. After a 5-min rinse with tap water, followed by a 5-min immersion in hematoxylin solution. Subsequently, the sections were rinsed with running water for 5 min. The sections were briefly immersed in 70% ethanol containing hydrochloric acid (Wako Pure Chemical Industries, Ltd.) for 2 sec to differentiate between hematoxylin and eosin staining. They were followed by another 5-min rinse in running water. The sections were immersed in eosin solution for 5 min. Afterward, the sections were sequentially washed with 3 times 100% ethanol and 3 times 100% xylene (Fuji film-wako, Osaka, Japan) for 5 min each. Imaging was conducted using an Olympus BX51 optical microscope.

### **III. Results**

#### **Visualization of A $\beta$ proteoforms in AD brains by MALDI-MSI**

To determine the accurate primary sequence of A $\beta$  in plaques has been a big challenge because of the heterogeneity within the terminal regions of A $\beta$ . This was due to the limitation of previously common protein sequencing by Edman sequencing, due to an in accessible N-terminus that hence resulted in inconsistent findings regarding the primary structure of plaque associated A $\beta$  peptides [26]. The advent of biological mass spectrometry (BMS) techniques has helped to significantly advance our understating of A $\beta$  plaque chemistry [1, 4, 5]. By our previous protocol, single ion images of the individual A $\beta$  peptides observed with MALDI-MSI were almost assigned to A $\beta$  species [17, 20]. To assess the reproducibility of our previous findings, we collected second cohort of patients that included 3 normal controls and 3 AD cases (Table 1). In this study, we used matrix-assisted laser desorption/ionization trapped ion mobility spectrometry time-of-flight based mass spectrometry imaging (MALDI timsTOF-flex) in combination with LC-MS/MS to probe both the proteomic and the lipidomic microenvironment associated with structural polymorphism of A $\beta$  plaques in sporadic AD patients. This system is superior to obtain precise  $m/z$  number to discriminate between

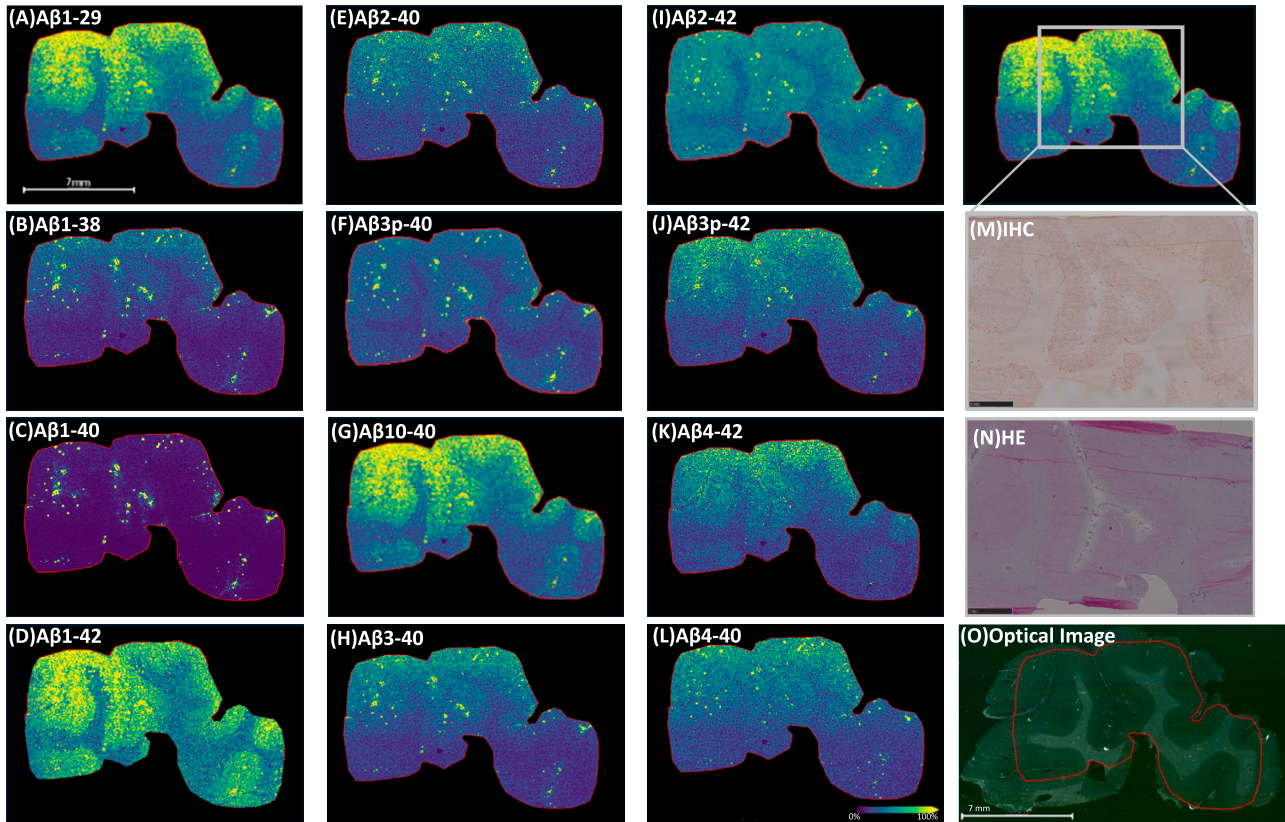


**Fig. 1.** MALDI-MSI for frozen AD brain section (Case 1). Various C-terminal and N-terminal truncated A $\beta$  peptides in AD occipital lobe cortex. From A) to O): A) Ab 1-29, B) 1-38, C) 1-40, D) 1-42, E) 2-40, F) 3p-40, G) 10-40, H) 3-40, I) 2-42, J) 3p-42, K) 4-42, L) 4-40, M) Immunohistochemistry of anti Ab antibody (82E1). N) HE staining, and O) Optic image of occipital lobe from AD Case 1. Bar = 7 mm.

crowded peptides coming from native A $\beta$  peptides such as A $\beta$ 11p-42, 1-29 and 10-40 as described below.

In the present study, A $\beta$ 1-40 distributes mostly along leptomeningeal large arterial vessels and parenchymal small arterioles, which is consistent with our previous finding. In addition, this topological pattern of A $\beta$ 1-40 is identical among most of shorter C-terminal truncated proteoforms including A $\beta$ 1-37, 38, and 39 (Figs. 1, 2 and Supplementary Fig. S1). By contrast, A $\beta$ 1-42 distributes in both leptomeningeal and parenchymal vasculatures as well as parenchymal plaque formation. In control brains, discrete A $\beta$ 1-40 nor 1-42 peptides were not detectable in Supplementary Fig. S3.

In the current study, N-terminally truncated A $\beta$ 43, A $\beta$ 2-43 and A $\beta$ 3p-43 was detected as native A $\beta$  proteoforms which is shown in Supplementary Fig. S2, rarely described so far. The removal of the first two residues (Asp and Ala) from A $\beta$  followed by cyclization of the third residue (Glu) to a pyroglutamate (forming N3pE-A $\beta$ ) are predominant N-terminal modifications of A $\beta$  species [28]. These were primarily detected in AD cerebral cortex extracts and were found to be localized in diffuse plaques in AD and Down Syndrome (DS) brain tissues much earlier than the standard A $\beta$  bearing the first amino-terminal residue. In this study, both peptide distribution is similar in

that mostly deposited in leptomeningeal vessels with smaller vessels in parenchyma. However, there seems a minor difference between distribution of these two peptides: while A $\beta$ 3p-43 distribution is a little bit dominant in parenchymal area than large leptomeningeal vasculatures and A $\beta$ 2-43 distribution is vice versa.

Interestingly, with advanced accurate mass spectrometry, we have detected and differentiated A $\beta$ 1-29 and A $\beta$ 10-40 as native A $\beta$  proteoforms from AD patients' brains and their distributions were found to be quite similar with A $\beta$ 1-42 (Figs. 1, 2 and Supplementary Fig. S1). As previously reported, trypsinization of A $\beta$  peptides yielded N-terminal truncated A $\beta$  includes A $\beta$ 1-28 theoretically. However, it is also possible to obtain A $\beta$ 1-29 because elastase cuts between G29 and A30 where a loose turn structure not making intermolecular  $\beta$ -sheet conformation. Furthermore, one possible explanation for A $\beta$ 1-29, A $\beta$ 10-40, and A $\beta$ 1-42 revealed similar distribution in AD brains is that they shared toxic turn formation at positions 22 and 23 which were deduced from the systematic proline replacement in full-length A $\beta$ 40 and A $\beta$ 42, respectively [31]. The presence of the toxic turn was also supported by the solid-phase nuclear magnetic resonance (NMR) analyses of the A $\beta$ 42 aggregates *in vitro* and the cryo-EM analysis of the A $\beta$ 42 aggregates from AD brain [11].

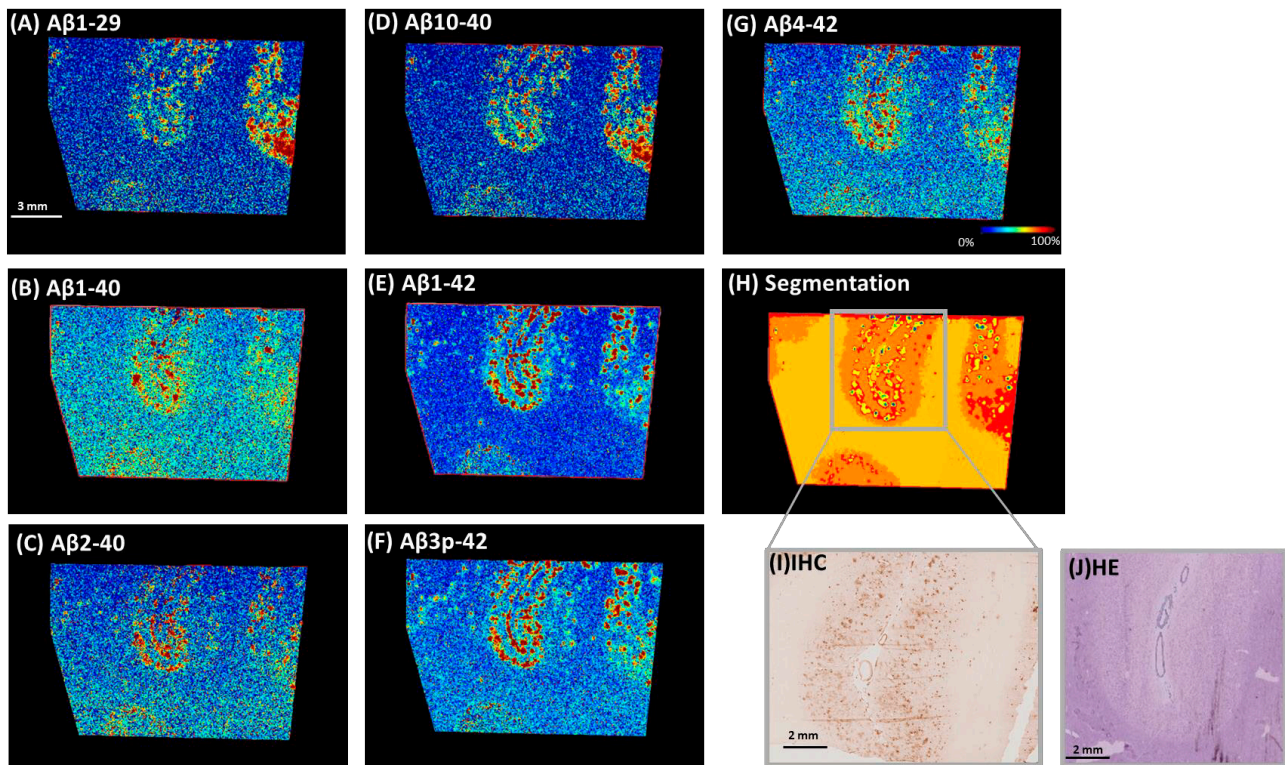


**Fig. 2.** MALDI-MSI for frozen AD brain sections (Case 2). Various C-terminal and N-terminal truncated A $\beta$  peptides in AD occipital lobe cortex. From **A**) to **J**): **A**) A $\beta$  1-29, **B**) 1-40, **C**) 2-40, **D**) 10-40, **E**) 1-42, **F**) 3p-42, **G**) 4-42, **H**) Segmentation data, Circled square was enlarged and showed **(I)** Immunohistochemistry of anti A $\beta$  antibody (82E1), and **(J)** HE staining, from AD Case 2, occipital lobe. Bar = 2 mm.

Among the different N-truncated A $\beta$  forms, A $\beta$ 4-42 was found to be the major A $\beta$  species in parenchymal A $\beta$ -plaques which is documented by our previous study [17, 20]. In Figs. 1, Fig. 2 and Supplemental Fig. S1, N-terminal truncation of full-length A $\beta$  between E3 and F4, as a naturally occurring proteoforms of A $\beta$ 40 and A $\beta$ 42 was also detected in the current study.

Localization of A $\beta$ 6-40 and A $\beta$ 6-42 has been described in our previous study of MALDI-MSI for human autopsied brain tissues [20]. Interestingly, distribution of A $\beta$ 6-40/42 is remarkably wide-spread in grey matter of AD patients' brains with a sharp contrast with other N-truncated form of A $\beta$  including A $\beta$ 2-40/42, 3(p)-40/42, 4-40/42, and 5-40/42. Although the intensity of the signals from A $\beta$ 6-40/42 of AD brains in the current study is not so strong with our previous data as shown in Supplementary Fig. S1, above-mentioned wide-spread tendency was clearly reproduced.

#### ***Laser microdissection based spatial in-depth proteomics of AD brains***

Laser microdissection (LMD) is widely used method to isolate minute amounts of tissue for subsequent proteomics analysis. An advantage of this technique is that a specific subset of tissue structures can be isolated and enriched from surrounding material. Here, we adopt LMD-

based method for the isolation of human brain tissues from the AD brain using nano liquid chromatography (nano LC) mass spectrometry (MS) analysis. Using this approach, we detected more than 103 proteins in amyloid plaques from every LMD area from AD brains. In Fig. 3, results of detailed overlapped and differentiated protein number obtained with LMD-based in-depth proteomics were shown by Venn diagram. Synaptic degeneration is a prominent feature of AD both in humans and AD models of the disease. While many clinical trials are now focusing on the interactions between immune responses and neurons in AD, as opposed to focusing only on the reduction of A $\beta$  and tau levels, new synaptic biomarkers are being developed with the aim of aiding the earlier diagnosis of AD and distinguishing between people who will stay cognitively healthy as they age and people who will develop AD.

A growing body of evidence supports those soluble oligomeric forms of A $\beta$  may be the potential effectors of neuronal injuries and death in the early stages of AD. However, the molecular mechanisms associated with neuronal loss induced by soluble A $\beta$  remain to be elucidated. Because microtubule-associated proteins (MAPs) are responsible for the polymerization, stabilization, and dynamics of the microtubule network, we investigated whether MAPs might represent the intracellular targets that would enable us to explain the microtubule perturbation

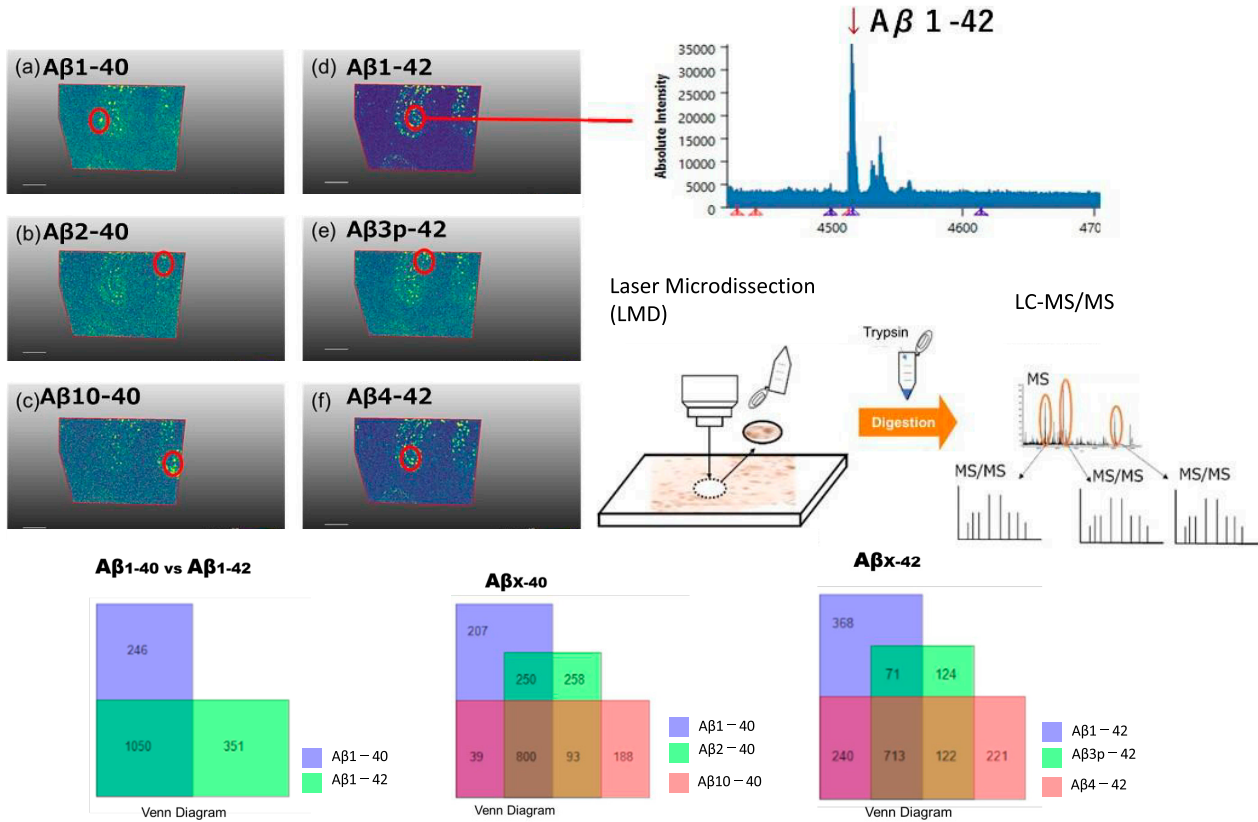


**Fig. 3.** Outflow of in-depth proteomics with laser captured microdissection. Venn diagram shows annotated number of proteins from Ab 1-40 and 1-42 (left), Aβ 1-40, 2-40, and 10-40 (middle), and 1-42, 3p-42, and 4-42 (right).

**Table 2.** Result of detected peptide fragments obtained from Aβ40 and Aβ42 specific deposited area

	(a) Aβ 1-40 deposition			(b) Aβ1-42 deposition		
	Score	Peptides	Sequence Coverage (%)	Score	Peptides	Sequence Coverage (%)
<b>SNCA</b>	368.9	8	51.8	389.7	6	52.3
<b>APOE</b>	1047.9	9	38.7	1098.2	10	39.5
<b>MAP1A</b>	1722.4	51	60.9	619.4	24	45.7
<b>MAP1B</b>	2363.7	69	50.7	1397.2	54	37.8
<b>MAP2</b>	1034.8	7	17.8	3298.4	24	38.3
<b>MAP4</b>	670.4	9	32.9	1087.4	10	34.5
<b>MAP6</b>	287.9	8	30.6	439.9	11	39.7
<b>Tau</b>	604.5	13	37.9	704.4	15	36.8

Focused proteins are SNCA, APOE, MAP1A, MAP1B, MAP2, MAP4, MAP6, and Tau. Ranking was performed with score reflecting detection sensitivity and intensity of the ions, peptide fragment count of the protein listed, and percentage coverage of the full length.

involved in soluble Aβ-mediated neuronal cell death. While Aβ and tau are the most well-studied contributors to synaptic degeneration in AD, we have focused on microtubule binding proteins including MAP1A, MAP1B, MAP2, MAP4, and MAP6 in addition to tau in Table 2. Interestingly, dendritic markers such as MAP2 was dominantly and stably co-localized with LMD samples from Aβ42 deposition and proteomic profiles representative of Aβ40 deposition is characterized with increased MAP1A and MAP1B fragments, possibly representing Aβ mediated synaptic dis-

organization process [41]. The current strategy of targeting Aβ proteoforms together with in-depth proteomics from postmortem brain tissues may expand key molecules to unravel neurotoxicity of Aβ and its toxic conformer state, for example, MAP1A, MAP1B and MAP2.

#### **Integrating shotgun proteomics and MALDI-MSI with on tissue digestion**

Shotgun analysis for trypsin digested tissue extracts was further introduced for human autopsy brain samples

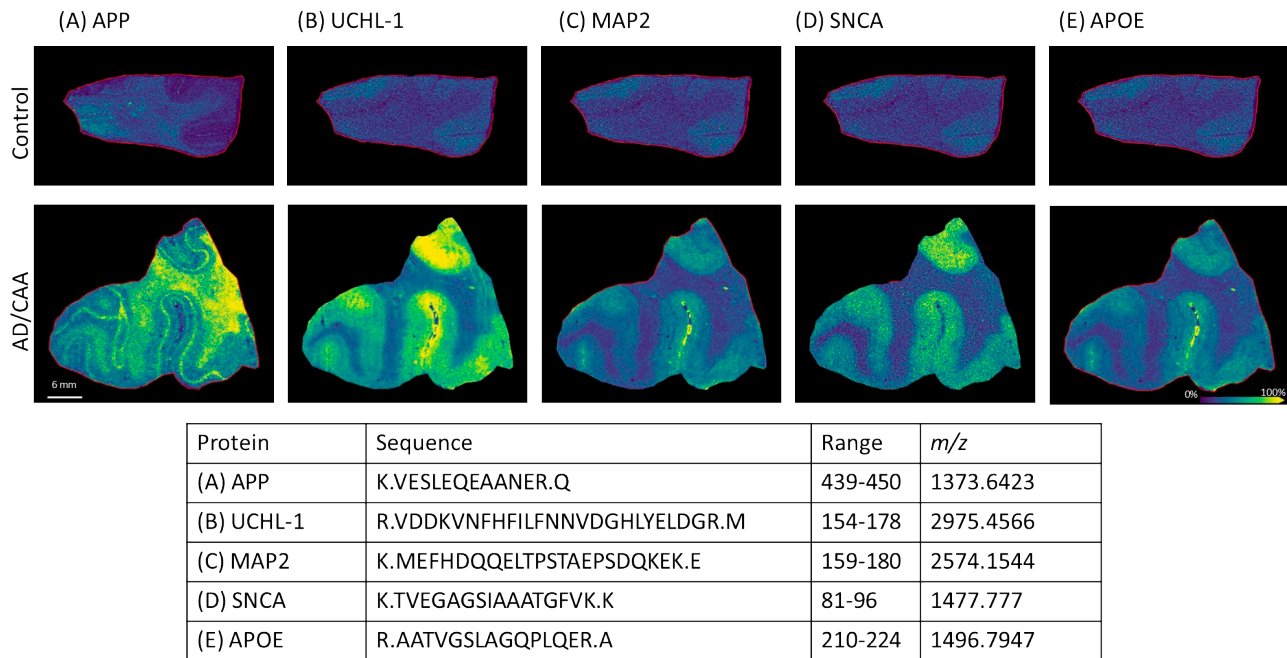


**Fig. 4.** Integrated MALDI-MSI and shotgun proteomics with LC-MS/MS. Visualization of APP, APOE, SNCA, UCHL1, and MAP2 proteins were differentially visualized with AD (Case 2; lower panel) and Control (Case 1; upper panel) brain. Visualization of the peptides derived from each protein are (A) APP: K. VESLEQEAAANER.Q, *m/z* 1373.6423, (B) UCHL-1: R. VDDKVNHFHILFNNVDGHLIELDGR.M, *m/z* 2975.4566, (C) MAP2: K. MEFHDQQELTPSTAEPDQKEK.E, *m/z* 2574.1544, (D) SNCA: K. TVEGAGSIAAATGFVK.K, (E) APOE: R. AATVGLAGQPLQER.A, *m/z* 1496.7947.

[32, 33]. A system equipped with Parallel Accumulation – Serial Fragmentation (PASEF) for LC-MS/MS shotgun analysis was applied to perform high-sensitivity and high-speed mass analysis. As a result, proteins at the order of  $10^3$  and peptides at the order of  $10^4$  were detected per sample as shown in Fig. 4. Fragments of proteins detected only in AD brains were sorted from the raw data sets and ranking was calculated based on a score value that comprehensively reflected detection sensitivity, intensity, peptide fragment count, coverage of the full length, error rate, and other factors.

Generally, molecules with higher score values are considered more reliable. Approximately 12,000 AD-specific peptide fragments were identified. By integrating the pathologically specific peptide list obtained from shotgun analysis with specific single peaks *in situ* on imaging tissues, a vast number of protein lists were effectively filtered. Among these proteins annotated, the top 50 fragments were extracted. Additionally, on tissue digestion was performed for MALDI-MSI, and a receiver operating characteristic (ROC) analysis was conducted on inter-sample peaks to elect single peaks specific to AD brains. The *m/z* values of AD-dominant peaks picked on imaging tissues and the *m/z* values of fragments obtained from the extract were compared, and visualization of each peptide fragment was conducted. As a result, fragments of proteins known to be related to AD, such as APP, ubiquitin C-terminal hydrolase-1 (UCHL1), MAP2, alpha-synuclein (SNCA), and

apolipoprotein E (APOE), were selected and visualized from the top 50 AD-specific peptide fragments obtained from abovementioned calculations. For example, peptide fragments derived from APP were detected in white matter dominant and cortical layer specific way in AD brains, similar distribution pattern was noticeable in control brain with much weaker intensity.

#### Lipid imaging of AD brains

Lipid imaging was performed on the serial sections of abovementioned protein imaging of postmortem human brains. As a result, clear and sharp demarcation between white matter and grey matter as shown in Fig. 5 and Supplementary data were obtained. Especially, phosphatidylcholine delineates underlying detailed layered structure of cortices of occipital lobe. By contrast, cerebroside distribution is widely detected in white matter. Segmentation method was applied for AD and control brains, and we found that lipid profile in white matter from AD is discriminative with that from control brain.

In this study, we have succeeded in visualizing heme in both AD and control human brains. In both brains, heme distribution is reflecting large vessels in leptomenigeal areas and small vessels in parenchymal areas. In control brain, heme distribution is sharply traced with vascular structure, however, in AD brain, scattered dots derived from heme were observed especially in white matter. This can be a sign of microbleeds and or reflecting retarded

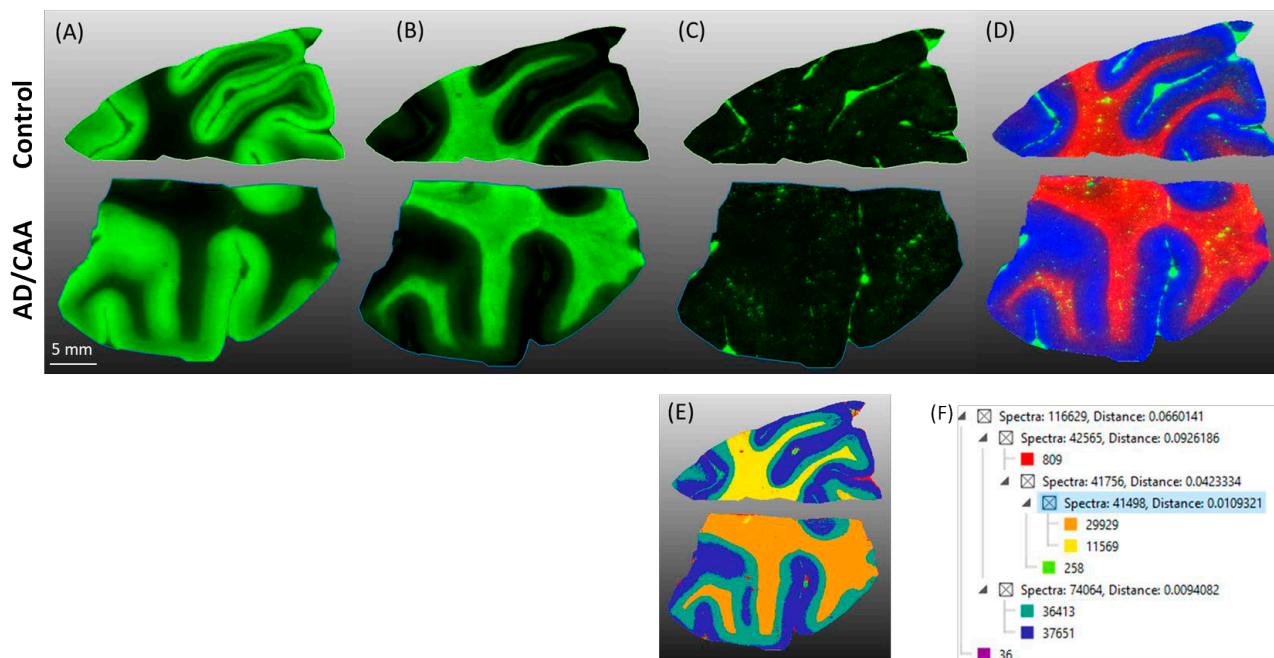


**Fig. 5.** Lipid imaging for frozen AD and control brains, occipital lobe with MALDIMSI. (A) to (D): Upper panel shows Control brain and lower panel shows AD brain. (A) Potassiated phosphatidylcholine 32:0, m/z 772. (B) Potassiated cerebroside, m/z 851 (C) Distribution of Heme B, m/z 616 was visualized with MALDI-MSI. (D) Merged figure. Red shows cerebroside, blue shows phosphatidylcholine, and green shows Heme. (E) Segmentation analysis for Control and AD brains. (F) Substructure of segmentation analysis shown in (E). Bar = 5 mm.

blood brain barriers. This needs further examination to be validated in the future study.

#### IV. Discussion

A $\beta$  has existed as various proteoforms in AD brains, and the focus has been on A $\beta$ 40 and A $\beta$ 42 at the C-terminus. A $\beta$ 42 aggregates rapidly and is highly toxic, and that A $\beta$ 43 is also highly toxic like A $\beta$ 42. As most of the reports relied simply on the analysis of protein extracts obtained from brain tissue and frozen brain using antibodies [30], it has been difficult to accurately distinguish the exact molecular weight and chemical modification of peptide fragments in a spatially resolved manner. Using the MALDI-MSI method, we explored A $\beta$  to the difference of one amino acid at a time and clarified the distribution of A $\beta$  in the postmortem brain for each molecular species [17, 20]. With this technology, we have originally identified the presence of A $\beta$ 1–41 and uniquely identified an antibody that specifically recognizes this molecule which was originally generated by us [17]. Most importantly, the MSI method revealed that A $\beta$ 1–42/43 and shorter A $\beta$ 1–36, 37, 38, 39, 40, and 41 had dramatically different distributions depending on the length of only one amino acid, such as perivascular or senile plaques [17, 20].

N-truncated A $\beta$  proteoforms of A $\beta$ 43 such as A $\beta$ 2–43 and A $\beta$ 3p–43 have been rarely detected in the previous studies. C-terminal variation of A $\beta$  peptides have been extensively discussed to hypothesize two alternative  $\gamma$ -

secretase-dependent product lines. APP is processed by  $\gamma$ -secretase at two  $\epsilon$ -sites and therefore generating two membranes bound A $\beta$  fragments A $\beta$ 49 and A $\beta$ 48, respectively. Then A $\beta$ 49 is converted into A $\beta$ 46 as the second catalytic step, which is converted into A $\beta$ 43 as the third catalytic step. According to this hypothesis, A $\beta$ 2–43 and A $\beta$ 3p–43 can be produced in line with A $\beta$ 1–43 production. Considering that N3pE-A $\beta$  showed faster aggregation kinetics [28], higher stability and increased neurotoxicity compared with full-length A $\beta$ , a minor difference in the distribution of two peptides observed in this study can be derived from peptide sequence—autonomous kinetics manner. Thus, N-terminally modified A $\beta$  peptides such as N3pE-A $\beta$  may represent better therapeutic targets than full-length A $\beta$ .

A $\beta$ 4-42 has been detected in postmortem brains from aged controls, patients with vascular dementia and AD patients by several groups [36, 44] and by us [17, 20]. By contrast, cerebrovascular amyloid was reported by Miller *et al.* [29] to contain mainly A $\beta$  peptides starting with residues 1 or 2. In this study, N-truncated proteoforms of A $\beta$  including A $\beta$ 2–40, 3(p)–40, 4–40, 5–40, 6–40, 7–40, 8–40, 9–40, and 11p–40 was visualized. Interestingly, distributions of A $\beta$ 4–40 was predominantly noticeable in parenchymal arterioles in comparison to large meningeal arterial vessels. In our previous study, above-mentioned distribution characteristics of A $\beta$ 4–40 was also noticeable in Supplementary Files [17]; A $\beta$ 4–40/42 species showed preferential localization within cerebral amyloid angiopa-

thy (CAA) and cored plaques, strongly suggesting poor clearance characteristics and consistent with the reduced solubility and enhanced oligomerization of their synthetic homologues. Furthermore, *in vivo* clearance studies demonstrated a fast brain efflux of N-terminally truncated and full-length monomeric forms whereas their oligomeric counterparts, particularly of A $\beta$ 4–40/42, consistently exhibited enhanced brain retention.

As for localization of A $\beta$ 6–40 and A $\beta$ 6–42, from the clinical standpoint of view, it is important to know that the N-terminal substitutions, KM670/671NL (Swedish), A2V, H6R (English), D7N (Tottori), and D7H (Taiwanese), are known as toxic mutations [15, 23]. These diseases are characterized by both increased A $\beta$  production and increased fibril formation. This suggests the possibility that these mutations appear not only to affect the total production but also to have a profound effect on the biophysical and toxic properties of the A $\beta$  peptides. Notably, the levels of protofibrils generated from D7N or H6R Ab were markedly inhibited despite enhanced fibril formation, N-terminal A $\beta$  mutations may accelerate amyloid fibril formation by a unique mechanism causing structural changes of A $\beta$  peptides. This is also highlighted that the increase in cross  $\beta$ -sheet structures of A $\beta$  correlated with cytotoxicity rather than the ability to form stable oligomers [6]. Furthermore, naturally occurring N-truncated or N-terminal mutated A $\beta$  peptide will have a profound effect on the biophysical and toxic properties in relation to metal binding property of His6.

Extensive studies of blood biomarkers reflecting A $\beta$ , tau, neurodegeneration and astrogliosis, have been developed and validated [2]. These markers, in particular, different variants of phosphorylated tau (p-tau), exhibit high performance in identifying AD pathology in the differential diagnosis of cognitive decline and demonstrate excellent prognostic performance to predict progression to AD dementia [2]. In addition, p-tau variants in blood have been validated against neuropathology exhibited at postmortem. As changes of plasma A $\beta$ 42/40 and p-tau are elevated in preclinical disease and might act as an integral enrichment aid for AD trials, it is not known which of several recently developed high-performing blood biomarkers has the best performance for clinical trial selection and monitoring in future clinical practice. The current strategy of targeting A $\beta$  proteoforms together with in-depth proteomics from post-mortem brain tissues may expand key molecules to unravel neurotoxicity of Ab and its toxic conformer state, for example, MAP1A, MAP1B and MAP2.

According to integrated MALDI-MSI and LC-MS/MS, APP distribution is visualized widely in white matter of AD brain as well as specific layer of grey matter where A $\beta$  proteoforms was noticeable in our intact MSI results above-mentioned. Together with AD dominant APP distribution, UCHL-1 distribution in grey matter of both control and AD brains were quite specific to the layer where A $\beta$  depositions is most prevailing in AD samples

(Fig. 4). The current observation described herein may indicate that altered ubiquitin signaling is an important component of AD pathogenesis through processing APP into A $\beta$ . As the current observation for APP and UCHL-1 were quite limiting in number and space, reproducibility trial will be necessary as the future experiments to be prepared [7, 25].

Under certain conditions, SNCA shows a marked alteration in its membrane-binding capacity. Following a conformational change, it tends to self-aggregate with other similarly pathologically misfolded SNCA molecules and with additional proteins, including ubiquitin [3]. This pathological shift seems to be the initial event in a certain neurodegenerative disease such as Parkinson Disease (PD) and asking how nerve cells rapidly eliminate the abnormal protein via ubiquitination and or proteasomal recycling is common feature shared with current A $\beta$  neurotoxicity.

As for microtubule-associated proteins, relatively macroscopic observation shown here by MAP2 distribution in grey matter as well as leptomeningeal vessel walls were significantly prominent in AD brains. This profile is quite similar with APOE distribution. Although there are arguments that integrating these two data sets obtained from MALDI-MSI and LC-MS/MS need to be integrated, several lines of evidence including our previous study [35] and others [34, 38] will convince pathological relevance of the current study.

Lipid metabolism is dysregulated in AD pathophysiology, but the connections between AD and lipid metabolic pathways are not fully understood. Mass spectrometry imaging (MSI)-based approach has been extensively introduced by Hanrieder *et al.* [13, 19, 21, 22, 28] to understand lipidomic alterations associated with A $\beta$  plaque pathology in genetic AD mouse models [19, 21, 22, 28] and post-mortem human brain [13]. Recently, Huang *et al.* has succeeded in visualizing spatial lipid patterns in human AD brain and genetic mouse models using desorption electrospray ionization (DESI)-based MSI integrated with imaging mass cytometry of correlative protein signatures [16]. Those spatial multi-omics experiments identify plaque-associated lipid metabolism that are dependent on progressing plaque pathology in both mouse models and the human brain.

Most importantly, we have succeeded in integrating multi-omics evidence to unravel molecular pathology of white matter in human postmortem brains. For example, we have succeeded in visualizing heme distribution in meningeal large vessels as well as parenchymal small vessels for both AD and normal brains. Of note, in white matter of AD, there is a scattered heme distribution possibly reflecting cerebral microbleeds. Heme has been proposed to interact with A $\beta$  and the formed A $\beta$ -heme complex exhibits peroxidase activity. Together with essential elements such as copper, zinc, and iron, heme bound to A $\beta$  may cause an enhanced cytotoxicity, which is emerging as a promising cytopathology in AD. This also motivated us to

develop multi-omics study including metallomics imaging by LA-ICP-MS and TOF-SIMS targeting essential elements of iron, copper and zinc in relation to A $\beta$  proteoforms in the future experiments.

## V. Conflicts of Interest

The authors declare that there are no conflicts of interest.

## VI. Acknowledgments

This work was supported by a Grant-in-Aid for Scientific Research (A) JSPS KAKENHI (Grant No. 23H00325 to K.I. and M.I.), JSPS KAKENHI (Grant No. JP 22H04923 (CoBiA) to Y.S. and S.M.), Integrated Research Initiative for Living Well with Dementia IRIDE) of the Tokyo Metropolitan Institute for Geriatrics and Gerontology IRIDE to Y.S., S.M., AMED (Grant No. JP21wm0425019 to Y.S., S.M.), MHLW Research on rare and intractable diseases Program (Grant No. JPMH23FC1008 to Y.S.) and by JST SPRING (Grant No. JPMJSP2129 to Y.T.). The authors declare that there are no conflicts of interest.

## VII. References

- Angel, M. P., Baldwin, S., Send, G. D., Sue, R. Y., Mayerf, E. J., Bichell, D., *et al.* (2017) Advanced in MALDI imaging mass spectrometry of proteins in cardiac tissue, including the heart valve. *Biochim. Biophys. Acta Proteins Proteom.* 1865; 927–935.
- Ashton, N. J., Janelidze, S., Mattsson-Carlgen, N., Binette, A. P., Strandberg, O., Brum, W. S., *et al.* (2022) Differential roles of A $\beta$ 42/40, p-tau231 and p-tau217 for Alzheimer's trial selection and disease monitoring. *Nat. Med.* 28; 2555–2562.
- Braak, H., Ghebremedhin, E., Rüb, U., Bratzke, H. and Tredici, K. (2004) Stages in the development of Parkinson's disease-related pathology. *Cell Tissue Res.* 318; 121–134.
- Caprioli, R. M., Farmer, T. B. and Gile, J. (1997) Molecular imaging of biological samples: Localization of peptides and proteins using MALDI-TOF MS. *Anal. Chem.* 69; 4751–4760.
- Caprioli, R. M. (2019) Imaging Mass Spectrometry: A Perspective. *J. Biomol. Tech.* 30; 7–11.
- Chikugo, A., Irie, Y., Tsukano, C., Uchino, A., Maki, T., Kume, T., *et al.* (2022) Optimization of the Linker Length in the Dimer Model of E22P-A $\beta$ 40 Tethered at Position 38. *ACS Chem. Neurosci.* 13; 2913–2923.
- Claes, B. S. R., Krestensen, K. K., Yagnik, G., Grgic, A., Kuik, C., Lim, M. J., *et al.* (2023) MALDI-IHC-Guided In-Depth Spatial Proteomics: Targeted and Untargeted MSI Combined. *Anal. Chem.* 95; 2329–2338.
- Colvin, M. T., Silvers, R., Ni, Q. Z., Can, T. V., Sergeyev, I., Rosay, M., *et al.* (2016) Atomic resolution structure of monomeric A $\beta$ 42 amyloid fibrils. *J. Am. Chem. Soc.* 138; 9663–9674.
- Enzlein, T., Cordes, J., Munteanu, B., Michno, W., Serneels, L., Strooper, B., *et al.* (2020) Computational Analysis of Alzheimer Amyloid plaque composition in 2D and Elastically Reconstructed 3D-MALDI MS Images. *Anal. Chem.* 92; 14484–14493.
- Frieg, B., Han, M., Giller, K., Dienemann, C., Riedel, D., Becker, S., *et al.* (2024) Cryo-EM structures of lipidic fibrils of amyloid- $\beta$  (1–40). *Nat. Commun.* 15; 1297.
- Gremer, L., Schölzel, D., Schenk, C., Reinartz, E., Labahn, J., Rvelli, R. B. G., *et al.* (2017) Fibril structure of amyloid- $\beta$  (1–42) by cryo-electron microscopy. *Science* 358; 116–119.
- Haass, C. and Selkoe, D. J. (2007) Soluble protein oligomers in neurodegeneration: lessons from the Alzheimer's amyloid  $\beta$ -peptide. *Nat. Rev. Mol. Cell Biol.* 8; 101–112.
- Hanrieder, J., Ljungdahl, A. and Andersson, M. (2012) MALDI Imaging Mass Spectrometry of Neuropeptides in Parkinson's Disease. *J. Vis. Exp.* (60); e3445.
- Hardy, A. J. and Higgins, A. G. (1992) Alzheimer's disease: the amyloid cascade hypothesis. *Science* 256; 184–185.
- Hori, Y., Hashimoto, T., Wakutani, Y., Urakami, K., Nakashima, K., Condon, M. M., *et al.* (2007) The Tottori (D7N) and English (H6R) familial Alzheimer disease mutations accelerate A $\beta$  fibril formation without increasing protofibril formation. *J. Biol. Chem.* 282; 4916–4923.
- Huang, H. X., Inglese, P., Tang, J., Yagoubi, R., Correia, G. D. S., Horneffer-van der Sluis, V. M., *et al.* (2024) Mass spectrometry imaging highlights dynamic patterns of lipid co-expression with A $\beta$  plaques in mouse and human brains. *J. Neurochem.* doi: 10.1111/jnc.16042. Epub ahead of print. PMID: 38372586.
- Ikegawa, M., Nirasawa, T., Kakuda, N., Miyasaka, T., Kuzuhara, Y., Murayama, S., *et al.* (2019) Visualization of Amyloid  $\beta$  Deposits in the Human Brain with Matrix-assisted Laser Desorption/Ionization Imaging Mass Spectrometry. *J. Vis. Exp.* (145); e57645.
- Irie, K. (2020) New diagnostic method for Alzheimer's disease based on the toxic conformation theory of amyloid  $\beta$ . *Biosci. Biotechnol. Biochem.* 84; 1–16.
- Jha, D., Blennow, K., Zetterberg, H., Savas, N. J. and Hanrieder, J. (2024) Spatial Neurolipidomics-MALDI mass spectrometry imaging of lipids in brain pathologies. *J. Mass Spectrom.* 59; e5008.
- Kakuda, N., Miyasaka, T., Iwasaki, N., Nirasawa, T., Wada-Kakuda, S., Takahashi-Fujigasaki, J., *et al.* (2017) Distinct deposition of amyloid- $\beta$  species in brains with Alzheimer's disease pathology visualized with MALDI imaging mass spectrometry. *Acta Neuropathol. Commun.* 5; 73.
- Kaya, I., Brinet, D., Michno, W., Baskurt, M., Zetterberg, H., Blennow, K., *et al.* (2017) Novel trimodal MALDI imaging mass spectrometry (IMS) at 10  $\mu$ m reveals spatial lipid and peptide correlates implicates in A $\beta$  plaque pathology in Alzheimer's disease. *ACS Chem. Neurosci.* 8; 2778–2790.
- Kaya, I., Zetterberg, H., Blennow, K. and Hanrieder, J. (2018) Shedding Light on the Molecular Pathology of Amyloid Plaques in Transgenic Alzheimer's Disease Mice Using Multimodal MALDI Imaging Mass Spectrometry. *ACS Chem. Neurosci.* 9; 1802–1817.
- Kechko, O. I., Adzubei, A. A., Tolstova, A. P., Indeykina, M. I., Popov, I. A., Zhokhov, S. S., *et al.* (2023) Molecular Mechanism of Zinc-Dependent Oligomerization of Alzheimer's Amyloid- $\beta$  with Taiwan (D7H) Mutation. *Int. J. Mol. Sci.* 24; 11241.
- Kollmer, M., Close, W., Funk, L., Rasmussen, J., Bsoul, A., Schierhorn, A., *et al.* (2019) Cryo-EM structure and polymorphism of A $\beta$  amyloid fibrils purified from Alzheimer's brain tissue. *Nat. Commun.* 10; 4760.
- Lim, M. J., Yagnik, G., Henkel, C., Frost, F. S., Bien, T. and Rothschild, J. K. (2023) MALDI HiPLEX-IHC: multiomic and multimodal imaging of targeted intact proteins in tissues. *Front. Chem.* 11; 1182404.
- Masters, C. L., Simms, G., Weinman, N., Multhaup, G., McDonald, B. and Beyreuther, K. (1985) Amyloid plaque core

- protein in Alzheimer disease and Down syndrome. *Proc. Natl. Acad. Sci. USA* 82; 4245–4249.
27. Masuda, Y., Uemura, S., Ohashi, R., Nakanishi, A., Takegoshi, K., Shimizu, T., *et al.* (2009) Identification of physiological and toxic conformations in A $\beta$ 42 aggregates. *Chembiochem* 10; 287–295.
  28. Michno, W., Nyström, S., Wehrli, P., Lashley, T., Brinkmalm, G., Guerard, L., *et al.* (2019) Pyroglutamation of amyloid- $\beta$ x-42 (A $\beta$ x-42) followed by A $\beta$ 1-40 deposition underlies plaque polymorphism in progressing Alzheimer's disease pathology. *J. Biol. Chem.* 294; 6719–6732.
  29. Miller, D. L., Currie, J. R., Iqbal, K., Potempska, A. and Styles, J. (1989) Relationships among the cerebral amyloid peptides and their precursors. *Ann. Med.* 21; 83–87.
  30. Moore, B. D., Chakrabarty, P., Levites, Y., Kukar, T. L., Baine, A., Moroni, T., *et al.* (2012) Overlapping profiles of A $\beta$  peptides in the Alzheimer's disease and pathological aging brains. *Alzheimers Res. Ther.* 4; 18.
  31. Morimoto, A., Irie, K., Murakami, K., Masuda, Y., Ohigashi, H., Nagao, M., *et al.* (2004) Analysis of the secondary structure of beta-amyloid (A $\beta$ 42) fibrils by systematic proline replacement. *J. Biol. Chem.* 279; 52781–52788.
  32. Nakagami, H., Sugiyama, N., Ishihama, Y. and Shirasu, K. (2012) Shotguns in the Front Line: Phosphoproteomics in Plants. *Plant Cell Physiol.* 53; 118–124.
  33. Nakagawa, T., Okumura, N., Ikegawa, M., Toyama, Y., Nirasawa, T., Mascarelli, F., *et al.* (2023) Shotgun proteomics identification of proteins expressed in the Descemet's membrane of patients with Fuchs endothelial corneal dystrophy. *Sci. Rep.* 13; 10401.
  34. Ogawa, M., Shintani-Domoto, Y., Nagashima, Y., Ode, K. L., Sato, A., Shimizu, Y., *et al.* (2020) Mass spectrometry-based absolute quantification of amyloid proteins in pathology tissue specimens: Merits and limitations. *PLoS One* 15; e0235143.
  35. Park, H., Yamanaka, T., Toyama, Y., Fujita, A., Doi, H. and Nirasawa, T. (2022) Hornerin deposits in neuronal intranuclear inclusion disease: direct identification of proteins with compositionally biased regions in inclusions. *Acta Neuropathol. Commun.* 10; 28.
  36. Rostagno, A., Cabrera, E., Lashley, T. and Ghiso, J. (2022) N-terminally truncated A $\beta$ 4-x proteoforms and their relevance for Alzheimer's pathophysiology. *Transl. Neurodegener.* 11; 30.
  37. Selkoe, D. J. and Hardy, J. (2016) The amyloid hypothesis of Alzheimer's disease at 25 years. *EMBO Mol. Med.* 8; 595–608.
  38. Shintani-Domoto, Y., Sugiura, Y., Ogawa, M., Sugiyama, E., Abe, H., Sakatani, T., *et al.* (2022) N-terminal peptide fragment constitutes core of amyloid deposition of serum amyloid A: An imaging mass spectrometry study. *PLoS One* 17; e0275993.
  39. Stoeckli, M., Staab, D., Staufienbiel, M., Wiederhold, K. and Signor, L. (2002) Molecular imaging of amyloid  $\beta$  peptides in mouse brain sections using mass spectrometry. *Anal. Biochem.* 311; 33–39.
  40. Trade, D., Schiffler, S., Becker, M., Wirtz, S., Steinhorst, K., Strehlow, J., *et al.* (2012) Exploring three-dimensional matrix-assisted laser desorption/ionization imaging mass spectrometry data: Three-dimensional spatial segmentation of mouse kidney. *Anal. Chem.* 84; 6079–6087.
  41. Tzioras, M., McGeachan, R. I., Durrant, C. S. and Spires-Jones, T. L. (2023) Synaptic degeneration in Alzheimer disease. *Nat. Rev. Neurol.* 19; 19–38.
  42. Wälti, M. A., Ravotti, F., Arai, H., Glabe, C. G., Wall, J. S., Böckmann, A., *et al.* (2016) Atomic-resolution structure of a disease-relevant A $\beta$  (1–42) amyloid fibril. *Proc. Natl. Acad. Sci. USA* 113; E4976–E4984.
  43. Williams, A. D., Portelius, E., Kheterpal, I., Guo, J. T., Cook, K. D., Xu, Y., *et al.* (2004) Mapping A $\beta$  amyloid fibril secondary structure using scanning proline mutagenesis. *J. Mol. Biol.* 335; 833–842.
  44. Wirths, O., Walter, S., Kraus, I., Klafki, H., Stazi, M., Oberstein, T., *et al.* (2017) Ntruncated A $\beta$ 4-x peptides in sporadic Alzheimer's disease cases and transgenic Alzheimer mouse models. *Alzheimers Res. Ther.* 9; 80.
  45. Xiao, Y., Ma, B., McElheny, D., Parthasarathy, S., Long, F., Hoshi, M., *et al.* (2015) A $\beta$  (1–42) fibril structure illuminates self-recognition and replication of amyloid in Alzheimer's disease. *Nat. Struct. Mol. Biol.* 22; 499–505.
  46. Yang, Y., Arseni, D., Zhang, W., Huang, M., Lövestam, S., Schweighauser, M., *et al.* (2022) Cryo-EM structures of amyloid- $\beta$  42 filaments from human brains. *Science* 375; 167–172.

---

This is an open access article distributed under the Creative Commons Attribution-NonCommercial 4.0 International License (CC-BY-NC), which permits use, distribution and reproduction of the articles in any medium provided that the original work is properly cited and is not used for commercial purposes.

---